Enhanced photocatalytic performance of $Bi_4O_5Br_2$ with three-dimensionally ordered macroporous structure for phenol removal

Kunfeng Zhang[1,2], Hongxia Chen[2], Wenbo Pei[3], Hongxing Dai[3], Junshan Li[4], and Yongfa Zhu[1] (✉)

[1] Department of Chemistry, Tsinghua University, Beijing 100084, China
[2] College of Environmental Engineering, Henan University of Technology, Zhengzhou 450001, China
[3] Department of Chemistry and Chemical Engineering, College of Environmental and Energy Engineering, Beijing University of Technology, Beijing 100124, China
[4] Institute for Advanced Study, Chengdu University, Chengdu 610106, China

ABSTRACT

Herein, a series of three-dimensionally ordered macroporous (3DOM) $Bi_4O_5Br_2$ photocatalysts with different macropore sizes were successfully fabricated via a polymethyl methacrylate (PMMA) template method. The photocatalytic activity for phenol degradation over 3DOM $Bi_4O_5Br_2$ first increased and then decreased with the rise in macropore size. Specifically, 3DOM $Bi_4O_5Br_2$-255 (macropore diameter ca. 170 nm) exhibits the best photocatalytic activity in the static system, which is about 4.5, 7.3, and 11.9 times higher than those of bulk $Bi_4O_5Br_2$, Bi_2WO_6, and g-C_3N_4, respectively. Meanwhile, high phenol conversion (75%) is also obtained over 3DOM $Bi_4O_5Br_2$-255 in the flow system under full spectrum irradiation. Furthermore, 3DOM $Bi_4O_5Br_2$-255 also shows strong mineralization capacity owing to the downward shift of valance band position (0.15 V) as compared with $Bi_4O_5Br_2$. Total organic carbon (TOC) removal rate over 3DOM $Bi_4O_5Br_2$-255 (62%) is much higher than that of $Bi_4O_5Br_2$ (17%). The enhancement in photocatalytic performance of 3DOM $Bi_4O_5Br_2$-255 is attributable to its better phenol adsorption, O_2 activation, and charge separation and transfer abilities. This work combines the advantages of 3D structure and surface dangling bonds, providing new possibilities for designing highly efficient photocatalysts for pollutants removal.

KEYWORDS

three-dimensionally ordered macroporous structure, $Bi_4O_5Br_2$, O_2 activation, photocatalysis, degradation

1 Introduction

Photocatalytic oxidation technology is a promising approach to convert organic pollutants in wastewater into CO_2 and H_2O by use of solar energy. However, the limited utilization of solar light, low degradation activity, and poor mineralization capacity restrict its practical application. In this concept, ideal photocatalysts should possess wide-range photoresponse, fast charge separation and transfer kinetics, deep valance band position, and abundant active sites [1–3]. The well-known photocatalysts TiO_2 and g-C_3N_4 have made a great breakthrough in the field of conversion of solar energy to hydrogen energy [4–8], but not in environmental remediation, owing to wide bandgap of TiO_2 and high valance band position of g-C_3N_4 [9, 10].

As promising photocatalysts for pollutant removal, bismuth-rich bismuth oxyhalides ($Bi_xO_yX_z$, X = Cl, Br, and I) with intrinsic internal electric field containing unique $[Bi_xO_y]$ and $[X_z]$ slices have attracted considerable attention in view of extraordinary electrical and optical properties, variable compositions, and stoichiometric ratios [11–15]. Among them, $Bi_4O_5Br_2$ with strong visible light response (bandgap energy (E_g) = 2.6 eV) and suitable redox potentials exhibits great potential [16]. However, relatively narrowed bandgap and large size of $Bi_4O_5Br_2$ lead to rapid recombination of photogenerated carriers and low charge transfer

efficiency. A variety of strategies such as surface modification, ion doping, morphology regulation, heterojunction construction, and defect engineering have been proposed to overcome its disadvantages [17–21]. Especially, developing ultrathin two-dimensional (2D) nanosheets is an effective way to improve charge separation and transfer efficiency by shortening the charge migration distance [22]. However, it is inevitable that bandgap widening because of the quantum size effect will lead to narrow photoabsorption range. The absorption edge of ultrathin $Bi_4O_5Br_2$ nanosheets showed obvious blue shift compared with bulk $Bi_4O_5Br_2$ (from 469 to 406 nm), which could not absorb visible light [23]. Meanwhile, the van der Waals interaction between the layers of 2D materials tends to cause irreversible stacking and agglomeration of nanosheets, which reduce the adsorption sites of pollutant and O_2 molecules [24]. To this end, researchers have developed three-dimensional (3D) $Bi_4O_5Br_2$ photocatalysts (flower-like microspheres and hollow spheres) to prevent agglomeration of ultrathin nanosheets and provide an interconnected open-framework to enhance photoabsorption efficiency [25–27]. Nonetheless, the barely satisfactory photocatalytic degradation performance needs further improvement due to insufficient sites for O_2 and pollutant molecule adsorption and activation.

Endowing photocatalysts with abundant dangling bonds by defect engineering is regarded as an effective approach to regulate

---

Address correspondence to zhuyf@mail.tsinghua.eud.cn

local geometric and electronic structure to influence the physical and chemical properties of photocatalyst [28]. $Mo_{1-x}S_{2-y}$ photocatalyst with Mo–S dangling bonds created by S vacancy enhanced the adsorption and activation for O_2. Meanwhile, the electrons are trapped to inhibit the recombination of photoexcited electron–hole pairs [29]. Pothole-rich WO_3 with dangling bonds also provided more active sites to anchor reactants, in which the formed dangling bonds can reduce the activation energy barrier [30]. Previous studies have demonstrated that superoxide radicals ($\cdot O_2^-$) are one of the main reactive species over $Bi_4O_5Br_2$ for phenolic pollutant oxidation [26, 31]. Thus, constructing $Bi_4O_5Br_2$ with dangling bonds is hypothesized to promote the activation of O_2 to accelerate the generation of reactive oxygen species (ROS) and simultaneously improve photogenerated charge separation efficiency. Recently, ordered macroporous BiOCl with similar structure to $Bi_4O_5Br_2$ was constructed, a large number of edge structures and Bi–O dangling bonds were formed over such 3D structure [32]. Furthermore, researchers have shown that three-dimensionally ordered macroporous (3DOM) photocatalysts have an advantage in solar light harvesting owing to multiple scatterings of light [33], such as 3DOM TiO_2 [34], 3DOM WO_3 [35], and 3DOM C_3N_4 [36]. Motivated by the above analysis, it could be expected that construction of 3DOM $Bi_4O_5Br_2$ with abundant dangling bonds would improve photocatalytic performance dramatically.

Herein, we report, for the first time, a polymethyl methacrylate (PMMA) colloidal crystal template method to construct a series of 3DOM $Bi_4O_5Br_2$ photocatalysts with different macropore sizes. The 3DOM $Bi_4O_5Br_2$ photocatalyst with macropore size of 170 nm possesses abundant surface Bi–O dangling bonds, which promote phenol adsorption, O_2 activation, charge separation and transfer, and light capturing abilities simultaneously. Highly efficient photocatalytic performance for phenol degradation is obtained. This work clearly shows the advantages and potentials of 3DOM photocatalysts and provides some guidance to develop efficient photocatalysts for environmental remediation.

2 Experimental

2.1 Materials

Bismuth nitrate pentahydrate ($Bi(NO_3)_3 \cdot 5H_2O$, 99.0%), ammonium oxalate (($NH_4)_2C_2O_4$, AO, 99.8%), and isopropyl alcohol (C_3H_8O, IPA, 99.7%) were purchased from Sinopharm Chemical Reagent Company. Critic acid ($C_6H_8O_7$, 99.5%) and ammonium bromide (NH_4Br, 99.0%) were supplied from Shanghai Aladdin Bio-Chem Technology Co., Ltd. Absolute ethanol (CH_3CH_2OH, 99.7%), ethylene glycol (($CH_2OH)_2$, EG, 99.0%), and anhydrous methanol (CH_3OH, MeOH, 99.5%) were purchased from Shanghai Titan Scientific Co., Ltd. Benzoquinone ($C_6H_4O_2$, BQ, 98.0%) and 5,5-dimethyl-1-pyrroline N-oxide ($C_6H_{11}NO$, DMPO, 97.0%) were supplied from TCI Development Company. All of the chemicals were used as received.

2.2 Preparation of 3DOM $Bi_4O_5Br_2$ with different macropore sizes

The well-arrayed PMMA microspheres with different diameters as the hard template were prepared according to reported literature with some modifications [37, 38]. Detailed preparation process is described in the Electronic Supplementary Material (ESM). In a typical procedure for preparation of 3DOM $Bi_4O_5Br_2$, 4.85 g of $Bi(NO_3)_3 \cdot 5H_2O$ and 2.10 g of citric acid were dissolved in a mixture of EG and MeOH with EG/MeOH volumetric ratio of 4:3 at room temperature. After vigorous stirred for 5 h, 0.60 g of NH_4Br was added to the above solution until a transparent

colorless solution was obtained. Subsequently, 2.00 g of PMMA was immersed into the above solution for 3 h. After filtered, the wet PMMA template with precursor was dried overnight at room temperature in a vacuum oven. Then the dried PMMA template with precursor was calcined in a tube furnace under static air at a ramp rate of 1 °C·min^{-1} from room temperature to 300 °C (holding for 2 h) and further to 425 °C (holding for 4 h), thus the 3DOM $Bi_4O_5Br_2$ photocatalyst was obtained. The 3DOM $Bi_4O_5Br_2$ photocatalysts with different macropore sizes were prepared by adjusting PMMA microspheres. According to the diameters of the as-synthesized PMMA microspheres, the 3DOM $Bi_4O_5Br_2$ photocatalysts are denoted as 3DOM $Bi_4O_5Br_2$-160, 3DOM $Bi_4O_5Br_2$-255, and 3DOM $Bi_4O_5Br_2$-380, respectively. For comparison, the bulk $Bi_4O_5Br_2$ photocatalyst was prepared using similar process to that of 3DOM $Bi_4O_5Br_2$ except that no PMMA template was used.

2.3 Photocatalysts characterization

X-ray diffraction (XRD) patterns were performed on a Rigaku (Japan) Smart-Lab X-ray diffractometer operated at 40 kV and 200 mA. Scanning electron microscopy (SEM) images were obtained on a Hitachi SU8000 microscope instrument. Transmission electron microscopy (TEM) images were obtained on a Hitachi HT7700 microscope. High-angle annular dark field scanning TEM (HAADF-STEM) images and energy-dispersive X-ray (EDX) spectroscopy elemental mappings were obtained on the equipment FEI G2 80–200/Chemi-STEM Cs-corrected TEM with probe corrector. Ultraviolet–visible diffuse reflectance spectroscopy (UV–vis DRS) images were measured on Agilent Cary 5000 spectrophotometer. X-ray photoelectron spectroscopy (XPS) images were recorded using Thermofisher ESCALAB 250Xi spectrometer. The Brunauer–Emmett–Teller (BET) surface area and pore-size distribution were measured using a Micromeritics ASAP 2020 Plus 2.00 analyzer. The photoluminescence (PL) spectra were recorded on Edinburgh FLS1000 fluorescence spectrometer with an excitation wavelength of 310 nm. Electron paramagnetic resonance (EPR) spectra were recorded on a JEOL-FA200 spectrometer. Surface photovoltage (SPV) spectra were obtained on a Zolix UOM-1S surface photovoltage spectrometer. Electrochemical measurements were performed on a CHI660E electrochemical workstation using a three-electrode cell system in a Na_2SO_4 aqueous solution (0.5 mol·L^{-1}). Pt wire and saturated Ag/AgCl were used as the counter electrode and the reference electrode, respectively. Zeta potentials were obtained on a HORIBA SZ-100 Zeta potential analyzer.

2.4 Photocatalytic performance evaluation

2.4.1 Photocatalytic performance evaluation in the static system

Photocatalytic activities of the as-obtained photocatalysts in the static system were evaluated in a multi-channel photocatalytic reactor (XPA-7, Xujiang Electromechanical Plant, Nanjing, China), as shown in Fig. S1 in the ESM. A 300 W Xe lamp was used as the light source. The light intensity was 330 mW·cm^{-2} measured by an optical power meter, and the spectral range of the Xe lamp was measured, as shown in Fig. S2 in the ESM. A cooling water circulation setup was used to keep the reaction temperature at 30 °C. In a typical photocatalytic procedure, 25 mg of the photocatalyst was dispersed in 50 mL of pollutant aqueous solution (5 mg·L^{-1} phenol, 10 mg·L^{-1} bisphenol A, and 5 mg·L^{-1} 2,4-dichlorophenol) by sonication for 5 min. Before illumination, the resulting suspension was stirred in the dark for 1 h to allow the system to establish the adsorption–desorption equilibrium. 2 mL of the suspension was taken out at given time intervals and filtered through a 0.22 μm nylon-66 membrane filter. The obtained

reaction solution was detected on a high-performance liquid chromatography (HPLC-20AT, Shimadzu) with a UV−vis detector and Restek C-18 column. The mobile phase was a mixture of acetonitrile and water (volumetric ratio = 40:60, 50:50, and 60:40) at a total flow rate of 1 mL·min⁻¹ and the detection wavelengths were 270, 270, and 284 nm, respectively. Total organic carbon (TOC) analysis was measured on a Jena Multi N/C 2100 TOC/TN spectrometer. Phenol conversion and TOC removal rates are defined as follows: phenol conversion (removal rate) = $(C_0 − C_t)/C_0$, where C_0 is the initial concentration and C_t is the concentration of reactant after a given reaction time (t).

2.4.2 Photocatalytic performance evaluation in the flow system

A home-made photocatalytic reactor (Fig. S3 in the ESM) was used to evaluate the photocatalytic degradation performance in the flow system. A typical process is as follows: 30 mg of photocatalyst was painted on a piece of aluminum foil. After dried at 60 °C for 10 h, the aluminum foil with photocatalyst was sealed in the reactor. Phenol aqueous solution (5 mg·L⁻¹) flowed through the reactor via a peristaltic pump. The reactor (7.0 cm × 2.5 cm) could hold about 20 mL of phenol aqueous solution and the flow rate could be controlled. The adsorption process was conducted in the dark and 2 mL of aqueous solution was collected at certain intervals. After the system reached the adsorption–desorption equilibrium, the photocatalytic reaction started with a 300 W Xenon lamp lighting on. Similarly, 2 mL of the reaction solution was collected at certain intervals and analyzed using the same way as in the static system.

2.5 Molecular O₂ activation test

100 μL of aqueous suspension of photocatalyst (5 g·L⁻¹) and 40 μL of 3,3',5,5'-tetramethylbenzidine (TMB, 50 mmol·L⁻¹) solution were added to 2 mL of HAc/NaAc buffer solution (pH = 4.8). A 300 W Xenon lamp equipped with a 420 nm cut-off filter was used as the light source. TMB oxidation performances (absorption wavelength at about 370 nm) over different photocatalysts and under different atmospheres (oxygen, air, and argon) were conducted and analyzed by UV−vis spectrophotometry. Meanwhile, in order to determine the type of ROS, TMB oxidation reaction was carried out using the same procedure in the presence of different scavengers.

3 Results and discussion

3.1 Construction of 3DOM Bi₄O₅Br₂ photocatalyst

The 3DOM Bi₄O₅Br₂ photocatalysts were synthesized by the citric acid assisted PMMA colloid crystal template method (Fig. 1(a)). Ordered PMMA microspheres with average diameters of 160, 255, and 380 nm were firstly obtained by assembling methyl methacrylate (MMA) monomers (Table S1 and Fig. S4 in the ESM) and were used as the colloidal crystal template. Then, a transparent precursor solution was immersed into the voids of PMMA microspheres, followed by filtration and drying procedures. After the calcination treatment at 425 °C under static air, the PMMA template was removed to obtain crystalline 3DOM Bi₄O₅Br₂. According to the thermogravimetric analysis (TGA, Fig.
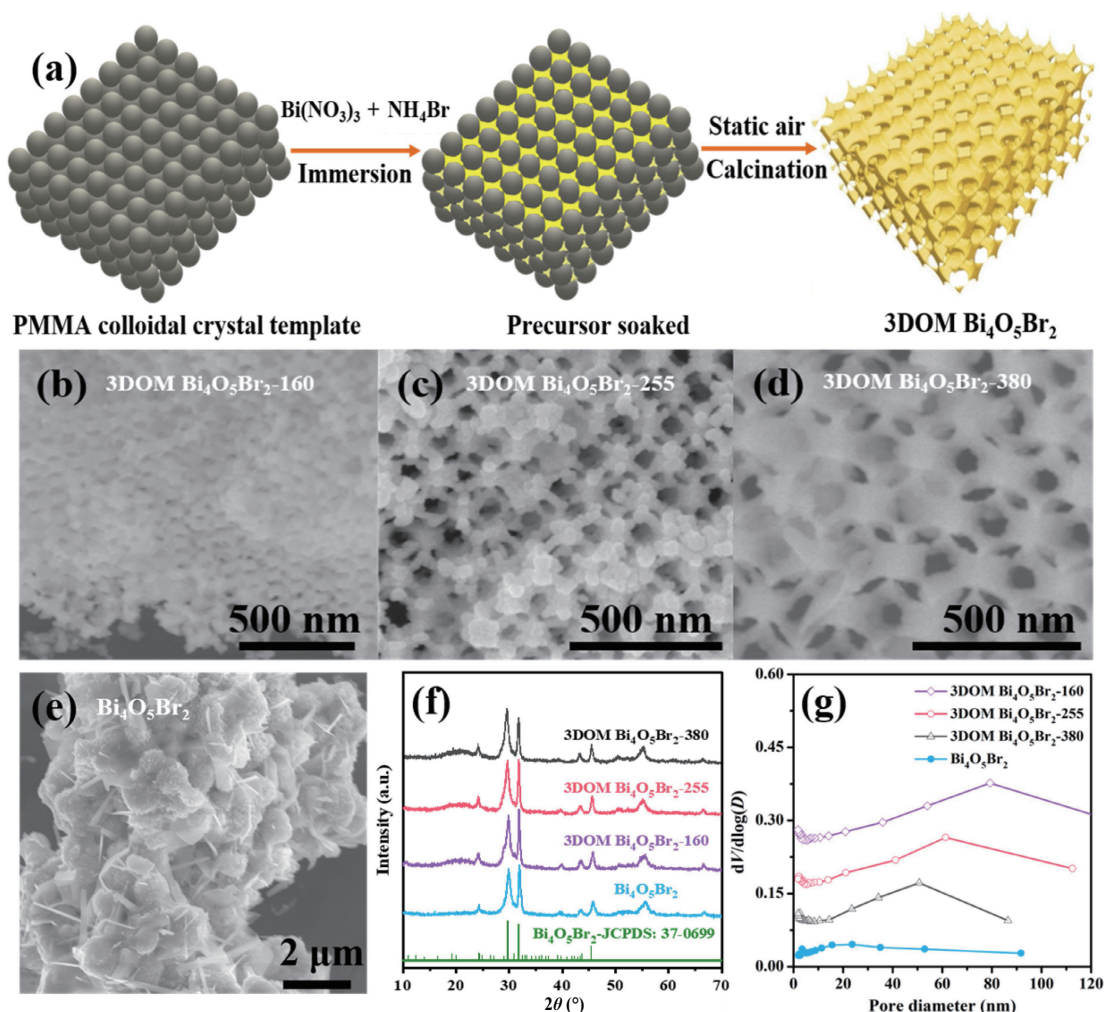
Figure 1 (a) Schematic illustration of the fabrication process for 3DOM Bi₄O₅Br₂. (b)–(e) SEM images, (f) XRD patterns, and (g) pore-size distributions of 3DOM Bi₄O₅Br₂-160, 3DOM Bi₄O₅Br₂-255, 3DOM Bi₄O₅Br₂-380, and Bi₄O₅Br₂.

S5 in the ESM), no obvious mass change was observed after 341 °C, indicating that PMMA template could be completely removed after calcination treatment under 425 °C for 4 h. Notably, critic acid as complexing agent played an important role in the formation of 3DOM structure. Only irregular $Bi_4O_5Br_2$ nanosheet was obtained when critic acid was not used. Furthermore, NH_4Br was superfluous with respect to $Bi(NO_3)_3 \cdot 5H_2O$ for specific stoichiometric ratio (1:2) in view of the fact that Br would lose during the calcination process.

The SEM images (Figs. 1(b)–1(d)) and Fig. S6 in the ESM) show that the samples display ordered 3D periodic porous structure with the macropore diameters of ca. 105, 170, and 255 nm, indicating that the formation of 3DOM $Bi_4O_5Br_2$. The macropore sizes of 3DOM $Bi_4O_5Br_2$-160, 3DOM $Bi_4O_5Br_2$-255, and 3DOM $Bi_4O_5Br_2$-380 show 34.4%, 33.3%, and 32.9% shrinkage compared with the PMMA microspheres, respectively. It should be noted that the ordered porous structures of 3DOM $Bi_4O_5Br_2$-255 and 3DOM $Bi_4O_5Br_2$-380 are both better than that of 3DOM $Bi_4O_5Br_2$-160, which can be explained by the fact that precursor infiltration is much harder for smaller PMMA microspheres [37, 39]. A typical sample of 3DOM $Bi_4O_5Br_2$-255 was investigated deeply. From Fig. S7(a) in the ESM, one can observe that the internal wall thickness of 3DOM $Bi_4O_5Br_2$-255 is only 7–11 nm. Generally, the thin architectural units are beneficial to shortening the carrier transfer distance and inhibiting the recombination rate of photoexcited electrons and holes [40]. The lattice fringes on the interconnection and interwall with the interplanar spacings of 0.302 and 0.325 nm are clearly observed from the high-resolution TEM (HRTEM) image (Fig. S7(b) in the ESM), which correspond to the (013) and (212) crystal planes of monoclinic $Bi_4O_5Br_2$, respectively. Furthermore, the HAADF-STEM image and the corresponding elemental mappings (Fig. S8 in the ESM) suggest the existence and uniform distribution of Bi, O, and Br elements over 3DOM $Bi_4O_5Br_2$-255. On the other hand, as shown in Fig. 1(e), the $Bi_4O_5Br_2$ photocatalyst exhibits irregular microsphere-like morphology with large sizes being 1–2 μm, and some nanorods are also observed. Obviously, the 3DOM $Bi_4O_5Br_2$-255 photocatalyst can expose more edge structures as compared with $Bi_4O_5Br_2$.

The XRD patterns (Fig. 1(f)) show that all of the samples exhibit strong intensities of diffraction peaks, indicating their good crystallinity. 3DOM and bulk $Bi_4O_5Br_2$ exhibit similar diffraction peaks and no other impurities are observed, suggesting the formation of pure phase, which can be indexed to monoclinic phase of $Bi_4O_5Br_2$ (JCPDS No. 37–0699). From pore-size distributions and N_2 adsorption–desorption isotherms of the samples (Fig. 1(g) and Fig. S9 in the ESM), the 3DOM $Bi_4O_5Br_2$ samples display typical type II isotherms with type H2 and H3 hysteresis loops. The H2 hysteresis loop at low relative pressure (p/p_0) of 0.4–0.8 comes from mesopores, and the H3 hysteresis loop at high p/p_0 of 0.8–1.0 is ascribed to macropores [41]. The mesopore and macropore result from accumulation of nanoparticles within a macroporous skeleton and open windows with a diameter of 30–90 nm [42]. The BET surface areas of the 3DOM $Bi_4O_5Br_2$ samples are in the range of 15.4–23.1 $m^2 \cdot g^{-1}$, while the BET surface area of $Bi_4O_5Br_2$ is only 5.2 $m^2 \cdot g^{-1}$. For 3DOM $Bi_4O_5Br_2$, the smaller the macropore size, the larger the BET surface area. Detailed results are also listed in Table S2 in the ESM. Generally, ordered porous structure and large surface area can enhance light trapping, mass transfer, and adsorption of pollutant molecules [37, 43]. Furthermore, 3DOM $Bi_4O_5Br_2$-255 possesses better hydrophilicity than that of $Bi_4O_5Br_2$, according to the results of water contact angle measurements (Fig. S10 in the ESM). The better hydrophilicity means the better dispersibility of photocatalyst in water, which can facilitate the contact between the photocatalyst and reaction solution [44].

From Fig. S11(a) in the ESM, one can observe that all of the samples can absorb UV and visible lights. The absorption edges of 3DOM $Bi_4O_5Br_2$-160, 3DOM $Bi_4O_5Br_2$-255, 3DOM $Bi_4O_5Br_2$-380, and $Bi_4O_5Br_2$ are 473, 478, 450, and 490 nm, respectively. Compared with $Bi_4O_5Br_2$, the absorption edges of 3DOM $Bi_4O_5Br_2$ display slight blue shift, which is attributed to the quantum confinement effect of thin internal wall of 3DOM $Bi_4O_5Br_2$ [39, 45]. It is worth noting that the 3DOM $Bi_4O_5Br_2$ samples exhibit stronger light absorbance below 365 nm than that of $Bi_4O_5Br_2$, owing to the multiple reflection and scattering of incident light inside the periodic porous structure [46]. According to the Kubelka–Munk function and their indirect band feature (Fig. S11(b) in the ESM), the E_g of 3DOM $Bi_4O_5Br_2$-160, 3DOM $Bi_4O_5Br_2$-255, 3DOM $Bi_4O_5Br_2$-380, and $Bi_4O_5Br_2$ are 2.63, 2.62, 2.78, and 2.50 eV, respectively. Afterwards, Mott–Schottky plots were conducted to measure the flat band potentials of 3DOM $Bi_4O_5Br_2$-255 and $Bi_4O_5Br_2$ under different frequencies. The flat-band potentials (Fig. S12 in the ESM) are determined to be −0.49 and −0.52 V (versus normal hydrogen electrode (vs. NHE)) for 3DOM $Bi_4O_5Br_2$-255 and $Bi_4O_5Br_2$, respectively. In general, the conduction band potential (E_{CB}) is approximately equal to the flat-band potential for n-type semiconductors [47]. Therefore, the valance band potentials (E_{VB}) of 3DOM $Bi_4O_5Br_2$-255 and $Bi_4O_5Br_2$ can be obtained based on the formula: $E_{CB} = E_{VB} - E_g$, which are 2.13 and 1.98 V (vs. NHE), respectively, as summarized in Table S3 in the ESM. Obviously, 3DOM $Bi_4O_5Br_2$-255 possesses much deeper valance band position, which is consistent with the results of XPS valance band spectra (Fig. S13 in the ESM). Similar result is observed over hierarchical porous BiOCl, which also shows more positive valence band than that of bulk BiOCl [48].

The surface elemental compositions and chemical states of the samples were investigated by XPS spectra. The C 1s signal at a binding energy of 284.8 eV was taken as the reference for calibration, no other elements were detected except Bi, Br, O, and C (Fig. S14(a) in the ESM). As shown in Fig. S14(b) in the ESM, the binding energies at 159.0–159.2 and 164.3–164.5 eV are assigned to the Bi $4f_{7/2}$ and Bi $4f_{5/2}$, respectively, which correspond to the surface Bi^{3+} species [49]. Different binding energies of Bi 4f for the two samples are due to different chemical environments of Bi^{3+} [50]. For Br 3d XPS spectra (Fig. S14(c) in the ESM), the peaks at 68.4–68.5 and 69.4–69.5 eV are attributed to Br $3d_{5/2}$ and Br $3d_{3/2}$, respectively, which are characteristic peaks of Br^- [18]. The O 1s XPS spectra in Fig. S14(d) in the ESM can be decomposed into two peaks at 529.9–530.1 and 531.3–531.4 eV, which are assigned to the surface lattice oxygen of Bi–O bonds and adsorbed oxygen species around oxygen deficient regions, respectively [51]. Obviously, the adsorbed oxygen concentration over 3DOM $Bi_4O_5Br_2$-255 (19.2%) is much higher than that of $Bi_4O_5Br_2$ (7.9%), indicating that 3DOM $Bi_4O_5Br_2$-255 possesses much more surface oxygen vacancies. In general, oxygen vacancies can contribute to the formation of trap state to capture electrons. The Bi 4f spectrum of 3DOM $Bi_4O_5Br_2$-255 exhibits a shift of 0.2 eV toward lower binding energy compared with that of $Bi_4O_5Br_2$, revealing the formation of Bi–O dangling bonds resulted from abundant oxygen vacancies [32]. To further confirm the existence and difference of surface oxygen vacancies, low-temperature EPR was conducted. As shown in Fig. S15 in the ESM, the two photocatalysts both display EPR signal at $g = 2.003$, which is attributed to the electrons trapped on oxygen defects [52, 53]. Meanwhile, 3DOM $Bi_4O_5Br_2$-255 exhibits stronger EPR signal than that of $Bi_4O_5Br_2$, suggesting that the former possesses more surface oxygen vacancies, which is consistent with the result of O 1s XPS spectra.

## 3.2 Boosting charge separation and transfer by 3DOM architecture

A series of spectral and photoelectrochemical characterizations were carried out to study the charge separation and transfer kinetics. From Fig. 2(a), one can see that 3DOM $Bi_4O_5Br_2$-255 and $Bi_4O_5Br_2$ show PL emission peaks at 510 and 525 nm under excitation with a wavelength of 310 nm, respectively. Compared with $Bi_4O_5Br_2$, 3DOM $Bi_4O_5Br_2$-255 shows a markedly lower PL emission intensity, implying a higher separation efficiency of photoexcited electron–hole pairs [54]. Moreover, as shown in Fig. 2(b) and Table S4 in the ESM, 3DOM $Bi_4O_5Br_2$-255 exhibits a longer transient fluorescence lifetime (9.65 ns) than that of $Bi_4O_5Br_2$ (7.04 ns), and the increased decay time further proves the more efficient exciton separation in 3DOM $Bi_4O_5Br_2$-255, which is originated from the trapping of more excited electrons by oxygen vacancies [52]. Figure 2(c) shows that the two samples exhibit positive surface photovoltage signals within the range of photoabsorption, suggesting that the photogenerated holes are the main carriers. Almost an order of magnitude increase of surface photovoltage for 3DOM $Bi_4O_5Br_2$-255 (202.2 μV) compared with $Bi_4O_5Br_2$ (24.5 μV) indicates that much higher number of photogenerated holes can transfer to the surface of 3DOM $Bi_4O_5Br_2$-255 to participate in oxidation reaction [30]. Electrochemical impedance spectroscopy (EIS) results (Fig. 2(d)) show that 3DOM $Bi_4O_5Br_2$-255 has lower electrochemical impedance than that of $Bi_4O_5Br_2$, which means a more efficient charge transport over 3DOM $Bi_4O_5Br_2$-255 [55]. The enhanced charge transfer efficiency is also confirmed by transient photocurrent responses in Fig. 2(e). The photocurrent density of 3DOM $Bi_4O_5Br_2$-255 is 3.2 times higher than that of $Bi_4O_5Br_2$. Furthermore, the surface charge density can also be determined by the zeta potential [56]. As shown in Fig. 2(f) and Table S5 in the ESM, the zeta potential of 3DOM $Bi_4O_5Br_2$-255 (51.7 mV) is 2.9 times higher than that of $Bi_4O_5Br_2$ (17.9 mV), which is in consistent with the result of transient photocurrent.

Based on the results, one can conclude that the oxygen vacancies over 3DOM $Bi_4O_5Br_2$-255 can serve as trapping sites for capturing photoexcited electrons, thus reducing the recombination rate of electron–hole pairs. Furthermore, the surface Bi/Br molar ratios of the samples were investigated by the XPS technique. As shown in Table S6 in the ESM, the surface Bi/Br atomic ratio of $Bi_4O_5Br_2$ (2.06) is close to corresponding stoichiometric ratio, while the Bi/Br atomic ratio of 3DOM $Bi_4O_5Br_2$-255 (2.39) is much higher than its stoichiometric ratio, indicating the bismuth-rich state of 3DOM $Bi_4O_5Br_2$-255. According to previous report [16], for $Bi_xO_yBr_z$, bismuth-rich state can strengthen the hybridization of the conduction band to improve the separation and transfer of photogenerated electron–hole pairs. Similar results are also obtained in this work. Meanwhile, due to the thin pore wall of 3DOM $Bi_4O_5Br_2$-255 and large size of $Bi_4O_5Br_2$, 3DOM $Bi_4O_5Br_2$-255 possesses much shorter charge transfer distance, thus an efficient charge transport pathway is established. In conclusion, charge separation and transfer efficiency are enhanced by 3DOM architecture, and excellent photocatalytic activity is expected to be obtained over 3DOM $Bi_4O_5Br_2$-255.

3.3 Highly efficient photocatalytic performance enhanced by 3DOM architecture

The photocatalytic activities of the as-prepared samples were first evaluated by photocatalytic degradation of phenol under visible light (> 420 nm) and full spectrum irradiation in the static system. Before light illumination, the phenol adsorption performance over the samples was investigated. As shown in Fig. 3(a), 3DOM $Bi_4O_5Br_2$ showed much stronger phenol adsorption capacity (0.39–0.57 mg·$g_{photocatalyst}^{-1}$) than that of $Bi_4O_5Br_2$ (0.03 mg·$g_{photocatalyst}^{-1}$), suggesting that more phenol pollutant molecules could be adsorbed on the surface of 3DOM $Bi_4O_5Br_2$ and participate in subsequent photocatalytic reaction. Accordingly, one can conclude that the photocatalyst with large surface area and abundant edge structure could provide more
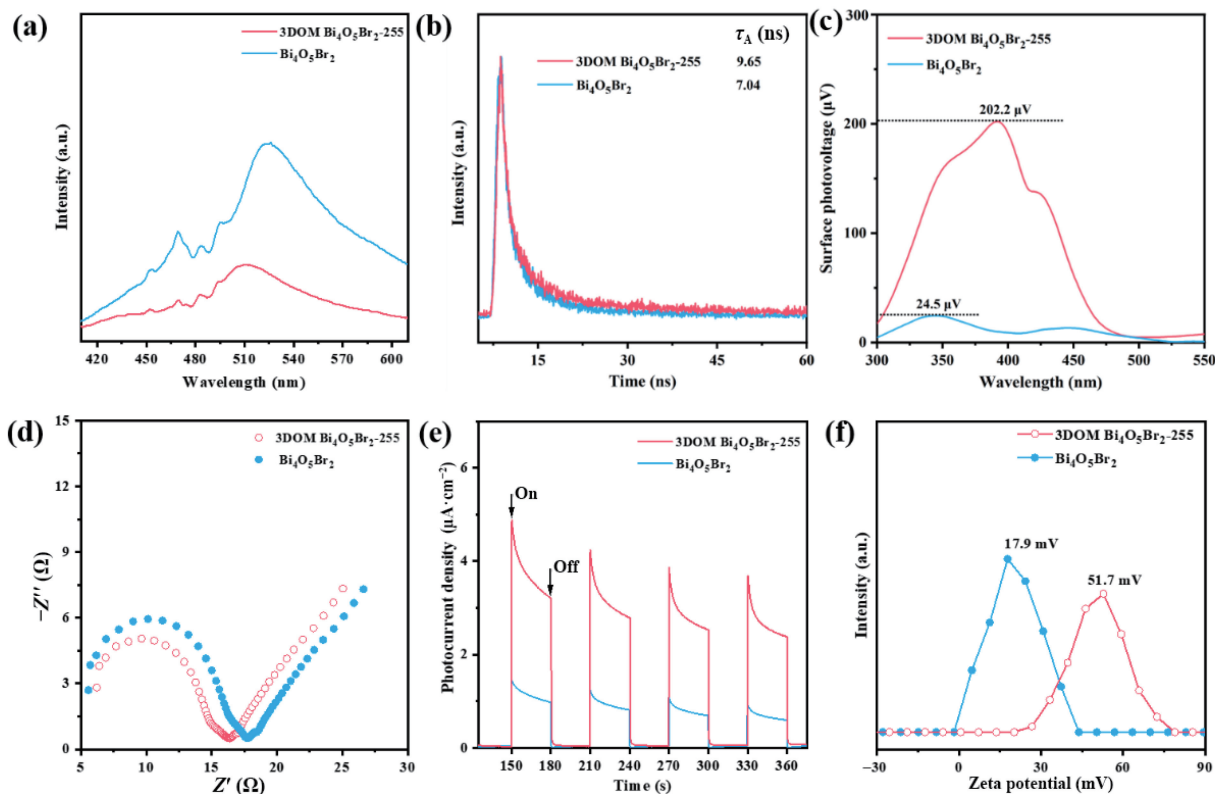
Figure 2 (a) Steady-state PL emission spectra, (b) time-resolved PL (TRPL) spectra, (c) SPV spectra, (d) EIS spectra, (e) transient photocurrent density plots, and (f) zeta potentials of 3DOM $Bi_4O_5Br_2$-255 and $Bi_4O_5Br_2$.
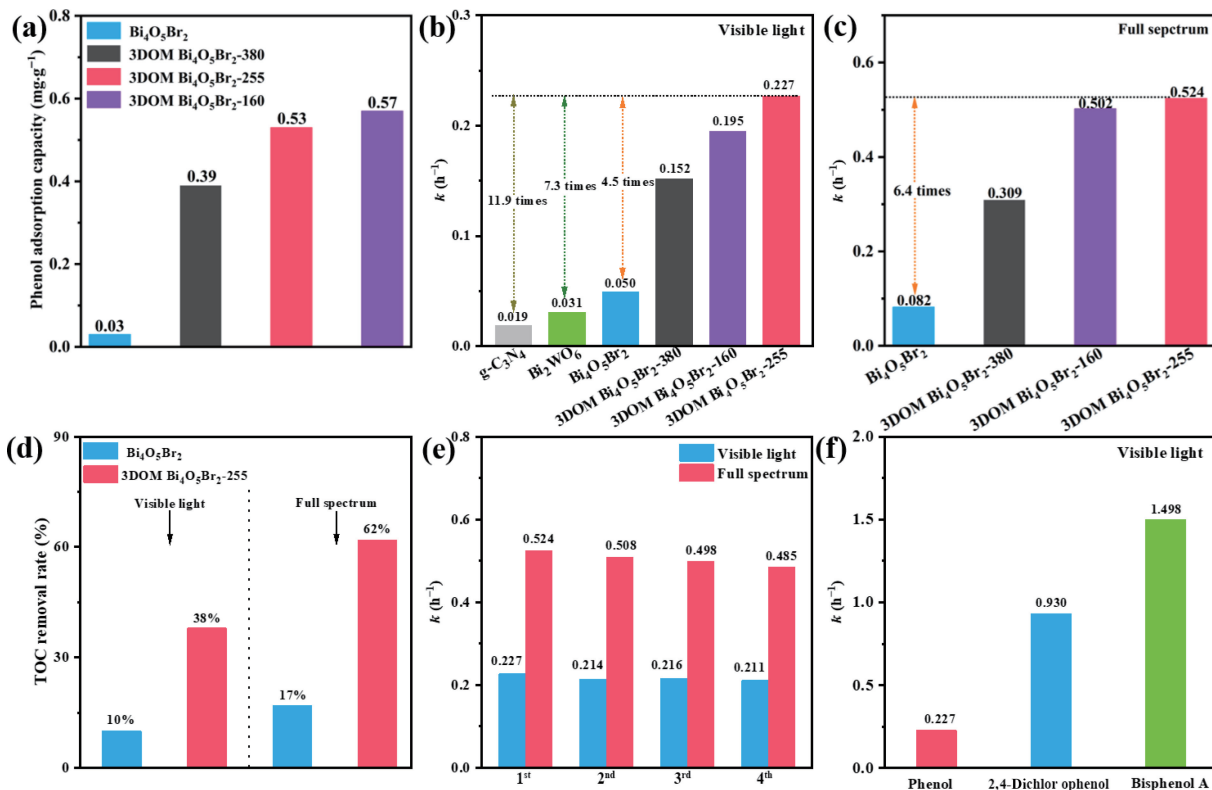
Figure 3 (a) Phenol adsorption capacity of 3DOM $Bi_4O_5Br_2$ composites and $Bi_4O_5Br_2$. (b) and (c) Photocatalytic phenol degradation performance in the static system under visible light and full spectrum illuminations over different photocatalysts. (d) TOC removal rates of 3DOM $Bi_4O_5Br_2$-255 and $Bi_4O_5Br_2$. (e) Recycling tests and (f) photocatalytic degradation of different phenols (phenol, bisphenol A, and 2,4-dichlorophenol) over 3DOM $Bi_4O_5Br_2$-255.

adsorption sites. For 3DOM $Bi_4O_5Br_2$, the smaller the macropore size, the stronger the phenol adsorption capacity. For comparison, Bi_2WO_6 and g-C_3N_4, the two most extensively studied visible-light photocatalysts were also evaluated. Obviously, the photocatalytic activities of the 3DOM $Bi_4O_5Br_2$ samples are much higher than that of $Bi_4O_5Br_2$ (Fig. 3(b)) and Fig. S16(a) in the ESM). The photocatalytic activity over 3DOM $Bi_4O_5Br_2$ first increased and then decreased with the rise in macropore size. Especially, 3DOM $Bi_4O_5Br_2$-255 with macropore size of 170 nm showed the best photocatalytic activity, about 60% phenol was degraded after 4 h of visible light illumination. Based on the pseudo-first order kinetics (Fig. S17 in the ESM), the reaction rate constant (k) of 3DOM $Bi_4O_5Br_2$-255 reached 0.227 h^{-1}, which was 4.5, 7.3, and 11.9 times higher than those of $Bi_4O_5Br_2$, Bi_2WO_6, and g-C_3N_4, respectively. Among 3DOM $Bi_4O_5Br_2$, 3DOM $Bi_4O_5Br_2$-255 possessed better photocatalytic activity than 3DOM $Bi_4O_5Br_2$-380 due to much stronger phenol adsorption and light trapping ability of the former. Though 3DOM $Bi_4O_5Br_2$-160 possessed larger surface area, the photocatalytic activity of 3DOM $Bi_4O_5Br_2$-160 was inferior to 3DOM $Bi_4O_5Br_2$-255, which could be explained that the mass transfer channel with macropore size of 170 nm was more conducive to the mass transfer of the photocatalytic reaction [38]. Moreover, 3DOM $Bi_4O_5Br_2$-255 also showed the best full spectrum activity (Fig. 3(c)) and Fig. S16(b) in the ESM), phenol conversion could reach about 90% and the photocatalytic activity was 6.4 times higher than that of $Bi_4O_5Br_2$. That is to say, compared with $Bi_4O_5Br_2$, 3DOM $Bi_4O_5Br_2$-255 also exhibited better ultraviolet light activity, which was in agreement with its stronger ultraviolet light absorption capacity. Also, the full spectrum activity of 3DOM $Bi_4O_5Br_2$-160 was close to 3DOM $Bi_4O_5Br_2$-255, which also indicated that the former possessed better ultraviolet light activity than the latter. Compared with $Bi_4O_5Br_2$ and $Bi_4O_5Br_2$ composite photocatalysts (Table S7 in the ESM) reported in the Refs. [17, 31, 57–59], 3DOM $Bi_4O_5Br_2$-255 also exhibited better photocatalytic performance than most of the reported photocatalysts.

Meanwhile, TOC removal rates (Fig. 3(d)) over 3DOM $Bi_4O_5Br_2$-255 reached 38% and 62% after 4 h of visible light and full spectrum illuminations, respectively, which were both much higher than those of $Bi_4O_5Br_2$ (10% and 17%), indicating stronger mineralization ability of 3DOM $Bi_4O_5Br_2$-255 for phenol. Recycling activity tests were conducted to investigate the photocatalytic stability of 3DOM $Bi_4O_5Br_2$-255. As shown in Fig. 3(e), no obvious deactivation emerged after four runs. By comparing the XRD patterns and XPS spectra of the fresh and used photocatalysts (Fig. S18 in the ESM), no significant changes were observed, indicating that the crystal structure and surface composition of 3DOM $Bi_4O_5Br_2$-255 were stable under the current reaction conditions.

In addition, we also investigated the photocatalytic activities of 3DOM $Bi_4O_5Br_2$-255 for other phenols, as shown in Fig. 3(f) and Fig. S16(c) in the ESM. Under visible light irradiation, 3DOM $Bi_4O_5Br_2$-255 showed better photocatalytic performance for bisphenol A and 2,4-dichlorophenol degradations. 2,4-Dichlorophenol conversion could reach 90%, while bisphenol A could be completely degraded after 2.5 h of visible light irradiation. The reaction rate constants of 0.930 and 1.498 h^{-1} were obtained for 2,4-dichlorophenol and bisphenol A degradations, respectively. Therefore, 3DOM $Bi_4O_5Br_2$-255 is an efficient photocatalyst for photocatalytic degradation of phenols.

In order to determine the main active species involved in this system, AO (0.01 mol·L^{-1}), IPA (0.01 mol·L^{-1}), and BQ (0.01 mmol·L^{-1}) were used to quench the photoinduced holes (h$^+$), hydroxyl radicals (·OH), and ·O_2^-, respectively [60, 61]. From Fig. 4(a), one can observe that the degradation efficiencies over 3DOM $Bi_4O_5Br_2$-255 all dropped with the addition of three kinds of scavengers. The photocatalytic activities were almost completely inhibited in the presence of AO and BQ, but phenol conversion slightly decreased when IPA was used, indicating that h$^+$ and ·O_2^- were responsible for the degradation of phenol.
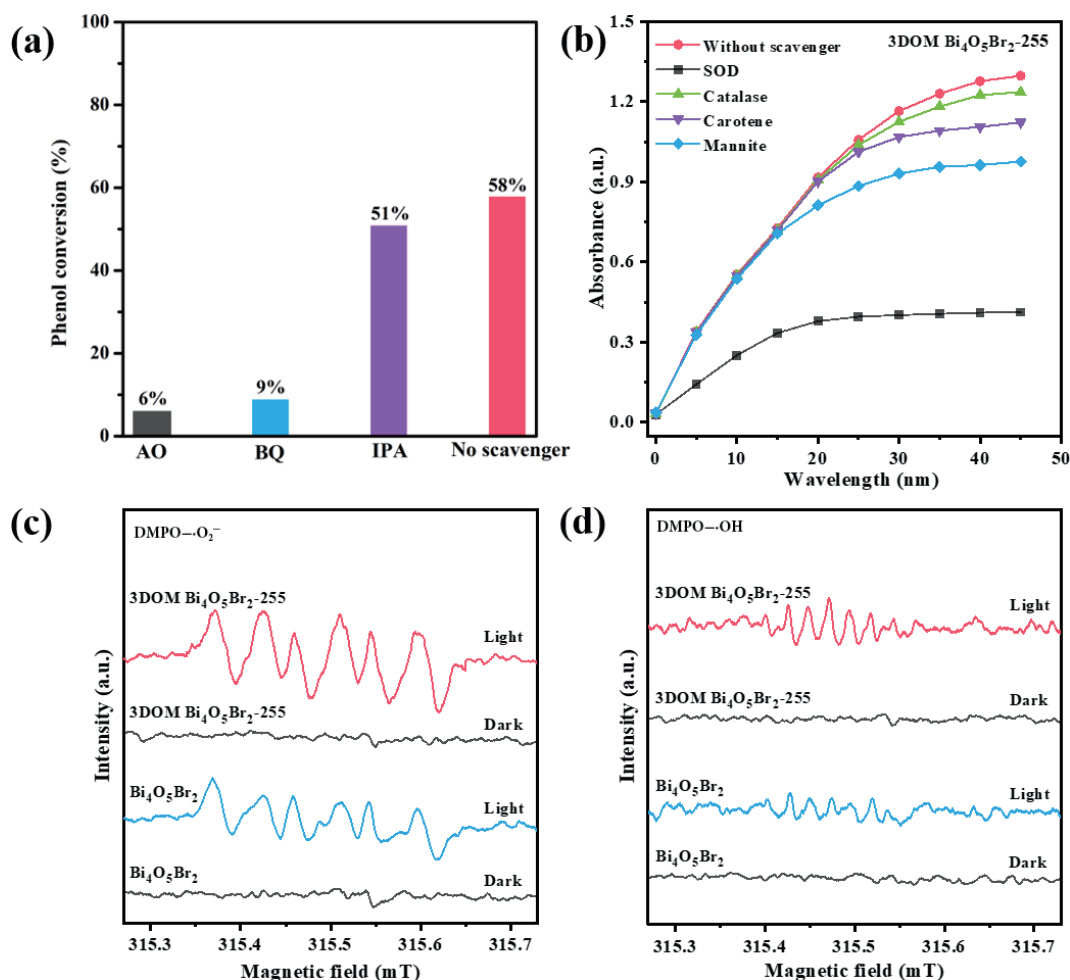
Figure 4 (a) Photocatalytic degradation of phenol and (b) TMB oxidation performance over 3DOM $Bi_4O_5Br_2$-255 in the presence of different scavengers. EPR spectra of (c) DMPO–·O_2^- and (d) DMPO–·OH over 3DOM $Bi_4O_5Br_2$-255 and $Bi_4O_5Br_2$.

Afterwards, TMB oxidation activity was evaluated to further investigate the ROS [62]. From Figs. S19(a) and S19(b) in the ESM, one can see that the absorbance of TMB oxidation products gradually increased with the extension of illumination time, suggesting the generation of ROS. The faster change trend of absorbance over 3DOM $Bi_4O_5Br_2$-255 indicated that 3DOM $Bi_4O_5Br_2$-255 possessed stronger O_2 activation ability than that of $Bi_4O_5Br_2$, which was mainly attributed to abundant surface Bi–O dangling bonds of 3DOM $Bi_4O_5Br_2$-255 [29]. Meanwhile, significantly different TMB oxidation rates under different atmospheres (O_2, air, and Ar) were observed (Figs. S19(c) and S19(d) in the ESM), $k_{O_2} > k_{air} > k_{Ar}$, which confirmed that O_2 was indispensable in TMB oxidation process and ROS was derived from O_2. To further identify the type of generated ROS during TMB oxidation, superoxide dismutase (SOD, 10 μL, 4000 U·mL^{-1}), catalase (10 μL, 4000 U·mL^{-1}), mannite (10 μL, 50 mmol·L^{-1}), and carotene (1 mg·mL^{-1}) were used as scavengers of ·O_2^-, hydrogen peroxide (H_2O_2), ·OH, and singlet oxygen ($^1O_2$), respectively [63, 64]. The results showed that TMB oxidation process was greatly suppressed with the addition of SOD, while the presence of the other three scavengers had little effects on TMB oxidation (Fig. 4(b)), confirming that ·O_2^- was the main ROS, which is in agreement with the quenching experiments.

Furthermore, EPR was conducted to directly detect the generated ROS. As shown in Fig. 4(c), much stronger DMPO–·O_2^- signals are observed over 3DOM $Bi_4O_5Br_2$-255 than that of $Bi_4O_5Br_2$. Given that ·O_2^- is mainly mediated by electrons ($e^- + O_2 \rightarrow ·O_2^-$) [65], the above result indicates that much more O_2 molecules could be activated by photogenerared electrons of

3DOM $Bi_4O_5Br_2$-255 as compared with $Bi_4O_5Br_2$. Owing to more oxygen vacancies over 3DOM $Bi_4O_5Br_2$-255, more trap states could form over 3DOM $Bi_4O_5Br_2$-255 [52], which could capture more electrons to active O_2 molecules, thus accelerating the generation of ·O_2^-. Meanwhile, relatively weak characteristic peaks of DMPO–·OH are observed (Fig. 4(d)), indicating that a large amount of ·O_2^- and a small amount of ·OH were generated under illumination. There are very weak signals of ·OH over the $Bi_4O_5Br_2$ sample, but relatively strong signals of ·OH are detected over 3DOM $Bi_4O_5Br_2$-255, which could be explained that 3DOM $Bi_4O_5Br_2$-255 possessed much deeper valance band position and faster charge separation and transfer efficiency. Based on the results of active species trapping experiments and EPR measurements, one can conclude that h$^+$ and ·O_2^- mainly participated in photocatalytic degradation reaction.

Therefore, the photocatalytic degradation process over 3DOM $Bi_4O_5Br_2$-255 most likely involves following steps, as illustrated in Fig. 5. (i) Phenol molecules are adsorbed on the surface of photocatalyst until reaching the adsorption–desorption equilibrium in the dark. (ii) The thin architectural units and the formed trap states due to oxygen vacancies can shorten charge transfer distance and capture excited electrons to inhibit recombination of the photogenerated electrons and holes pairs. Thus, more active charges can transfer to the surface of the photocatalyst and participate in the photocatalytic process. (iii) The e$^-$ and h$^+$ react with O_2 molecules and OH$^-$ to generate ·O_2^- and ·OH, respectively. (iv) Photogenerated h$^+$, ·O_2^-, and ·OH together attack pollutant molecules adsorbed on the surface of photocatalyst, oxidize them into other organic molecules, and finally mineralize them into CO_2 and H_2O.
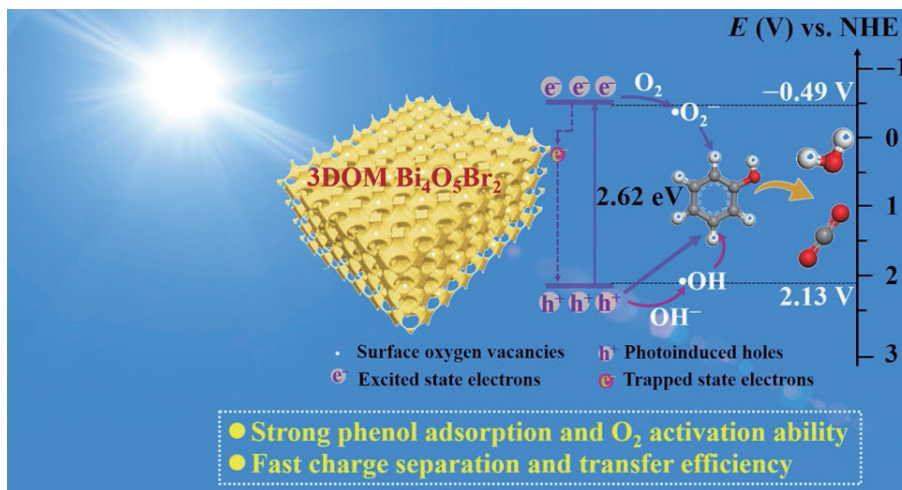
Figure 5 Schematic illustration of photocatalytic phenol removal over 3DOM Bi$_4$O$_5$Br$_2$-255.

For practical application, the photocatalytic activities of 3DOM Bi$_4$O$_5$Br$_2$-255 and Bi$_4$O$_5$Br$_2$ in the flow system were also evaluated. As shown in Fig. 6 and Fig. S18 in the ESM, phenol molecules first went through the dark adsorption process over photocatalysts in the flow system. For 3DOM Bi$_4$O$_5$Br$_2$-255, phenol could be completely adsorbed after 30 min of adsorption process, the adsorption–desorption equilibrium was established after 4 h, and 12% phenol adsorption rate was observed. For Bi$_4$O$_5$Br$_2$, 65% phenol at most could be adsorbed during the whole adsorption process, and the phenol adsorption rate was only 8% when the adsorption–desorption equilibrium was established. Under visible light illumination (Fig. S20(a) in the ESM), phenol was gradually degraded, phenol conversions over 3DOM Bi$_4$O$_5$Br$_2$-255 and Bi$_4$O$_5$Br$_2$ could keep 24% and 10% with the extension of reaction time, respectively. That is to say, the phenol degradation efficiency over 3DOM Bi$_4$O$_5$Br$_2$-255 was much higher than its adsorption rate, while the phenol degradation efficiency over Bi$_4$O$_5$Br$_2$ did not change significantly compared with the adsorption rate. Meanwhile, under full spectrum irradiation (Fig. 6(a)), 75% phenol conversion was obtained over 3DOM Bi$_4$O$_5$Br$_2$-255, while phenol conversion was only 27% for Bi$_4$O$_5$Br$_2$. Furthermore, 3DOM Bi$_4$O$_5$Br$_2$-255 also showed better photocatalytic performance than Bi$_4$O$_5$Br$_2$ under 1 sun illumination (100 mW·cm^{-2}). For Bi$_4$O$_5$Br$_2$, no obvious difference was observed before and after the light illumination, but phenol conversion could reach 20% over 3DOM Bi$_4$O$_5$Br$_2$-255 (Fig. 6(b)).

We also investigated the effect of flow rate (17.2, 34.3, and 68.6 L·h^{-1}·m^{-2}) on the photocatalytic performance of 3DOM Bi$_4$O$_5$Br$_2$-255 in the flow system. From Fig. S20(b) in the ESM, one can observe that phenol could be completely adsorbed during the dark adsorption process under different flow rates. When the flow rate was low (17.2 L·h^{-1}·m^{-2}), it took longer time (6 h) to reach the adsorption–desorption equilibrium and the phenol adsorption rate could reach 18%. With the rise in flow rate (68.6 L·h^{-1}·m^{-2}), the adsorption–desorption equilibrium was established after 2.5 h of adsorption process, but only 6% phenol adsorption rate was observed. Under visible light irradiation, phenol conversions were 41% and 11% at flow rates of 17.2 and 68.6 L·h^{-1}·m^{-2}, respectively. Obviously, with the increase of flow rate, the photocatalytic degradation activity decreased due to the shortened contact time between phenol and photocatalyst. Even so, high photocatalytic activity could be obtained via controlling the flow rate of system. Overall, 3DOM Bi$_4$O$_5$Br$_2$-255 exhibits excellent photocatalytic performance in the flow system, which possesses great potential to meet the practical application requirements.

4 Conclusions

In summary, we developed 3DOM Bi$_4$O$_5$Br$_2$ photocatalysts with abundant edge structures and oxygen vacancies. The 3DOM structure can provide more sites for phenol adsorption and O$_2$ activation, and simultaneously enhance charge separation and transfer efficiency. 3DOM Bi$_4$O$_5$Br$_2$-255 displays excellent photocatalytic performance for phenol removal, which is much
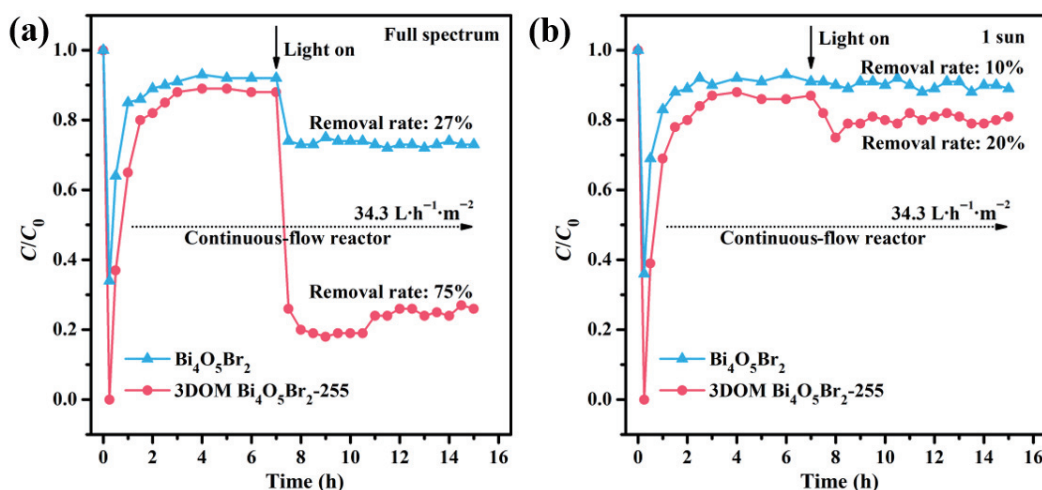
Figure 6 Photocatalytic activities for phenol degradation over 3DOM Bi$_4$O$_5$Br$_2$-255 and Bi$_4$O$_5$Br$_2$ in the flow system (34.3 L·h^{-1}·m^{-2}) under (a) full spectrum and (b) 1 sun illuminations.

higher than those of Bi₄O₅Br₂, Bi₂WO₆, and g-C₃N₄. Meanwhile, 3DOM Bi₄O₅Br₂-255 possesses strong mineralization capacity resulting from its deep valance band position. Moreover, 3DOM Bi₄O₅Br₂-255 also exhibits good stability during recycling experiments. This work provides some guidance on designing highly efficient photocatalysts via synergistically developing 3D structure and surface dangling bonds.

Acknowledgements

Electronic Supplementary Material: Supplementary material (further experimental details, reaction conditions of PMMA microspheres (Table S1 in the ESM), photocatalytic reactors (Figs. S1 and S3 in the ESM), spectral range of Xe lamp (Fig. S2 in the ESM), SEM images of PMMA microspheres (Fig. S4 in the ESM), TGA analysis of PMMA template (Fig. S5 in the ESM), SEM images (Fig. S6 in the ESM), HRTEM images, HAADF-STEM image and the corresponding elemental mappings (Figs. S7 and S8 in the ESM), N₂ adsorption–desorption isotherms and BET measurements (Fig. S9 and Table S2 in the ESM), contact angles (Fig. S10 in the ESM), UV–vis DRS spectra (Fig. S11 in the ESM), Mott–Schottky plots (Fig. S12 in the ESM), energy band structures (Table S3 in the ESM), XPS valence band spectra (Fig. S13 in the ESM), XPS spectra (Fig. S14 in the ESM), EPR spectra (Fig. S15 in the ESM), TRPL fitting results (Table S4 in the ESM), zeta potentials (Table S5 in the ESM), surface element compositions (Table S6 in the ESM), XRD patterns and XPS spectra after photocatalytic reaction (Fig. S18 in the ESM), O₂ activation test (Fig. S19 in the ESM), and photocatalytic performance (Figs. S16, S17, and S20, and Table S7 in the ESM) of typical samples) is available in the online version of this article at https://doi.org/10.1007/s12274-023-5582-5.

References

[1] Hoffmann, M. R.; Martin, S. T.; Choi, W.; Bahnemann, D. W. Environmental applications of semiconductor photocatalysis. *Chem. Rev.* **1995**, *95*, 69–96.

[2] Qu, Y. Q.; Duan, X. F. Progress, challenge, and perspective of heterogeneous photocatalysts. *Chem. Soc. Rev.* **2013**, *42*, 2568–2580.

[3] Tong, H.; Ouyang, S. X.; Bi, Y. P.; Umezawa, N.; Oshikiri, M.; Ye, J. H. Nano-photocatalytic materials: Possibilities and challenges. *Adv. Mater.* **2012**, *24*, 229–251.

[4] Fujishima, A.; Honda, K. Electrochemical photolysis of water at a semiconductor electrode. *Nature* **1972**, *238*, 37–38.

[5] Liu, J.; Liu, Y.; Liu, N. Y.; Han, Y. Z.; Zhang, X.; Huang, H.; Lifshitz, Y.; Lee, S. T.; Zhong, J.; Kang, Z. H. Metal-free efficient photocatalyst for stable visible water splitting via a two-electron pathway. *Science* **2015**, *347*, 970–974.

[6] Wang, X. C.; Maeda, K.; Thomas, A.; Takanabe, K.; Xin, G.; Carlsson, J. M.; Domen, K.; Antonietti, M. A metal-free polymeric photocatalyst for hydrogen production from water under visible light. *Nat. Mater.* **2009**, *8*, 76–80.

[7] Zhao, D. M.; Wang, Y. Q.; Dong, C. L.; Huang, Y. C.; Chen, J.; Xue, F.; Shen, S. H.; Guo, L. J. Boron-doped nitrogen-deficient carbon nitride-based Z-scheme heterostructures for photocatalytic overall water splitting. *Nat. Energy* **2021**, *6*, 388–397.

[8] Zhou, W.; Li, W.; Wang, J. Q.; Qu, Y.; Yang, Y.; Xie, Y.; Zhang, K. F.; Wang, L.; Fu, H. G.; Zhao, D. Y. Ordered mesoporous black TiO₂ as highly efficient hydrogen evolution photocatalyst. *J. Am. Chem. Soc.* **2014**, *136*, 9280–9283.

[9] Dong, H. R.; Zeng, G. M.; Tang, L.; Fan, C. Z.; Zhang, C.; He, X. X.; He, Y. An overview on limitations of TiO₂-based particles for photocatalytic degradation of organic pollutants and the corresponding countermeasures. *Water Res.* **2015**, *79*, 128–146.

[10] Fu, J. W.; Yu, J. G.; Jiang, C. J.; Cheng, B. g-C₃N₄-based heterostructured photocatalysts. *Adv. Energy Mater.* **2018**, *8*, 1701503.

[11] Li, J.; Zhang, L. Z.; Li, Y. J.; Yu, Y. Synthesis and internal electric field dependent photoreactivity of Bi₃O₄Cl single-crystalline nanosheets with high {001} facet exposure percentages. *Nanoscale* **2014**, *6*, 167–171.

[12] Li, R.; Xie, F. X.; Liu, J. X.; Wang, Y. W.; Wang, Y. F.; Zhang, X. C.; Fan, C. M. Synthesis of Bi₄O₅Br₂ from reorganization of BiOBr and its excellent visible light photocatalytic activity. *Dalton Trans.* **2016**, *45*, 9182–9186.

[13] Ji, M. X.; Di, J.; Liu, Y. L.; Chen, R.; Li, K.; Chen, Z. G.; Xia, J. X.; Li, H. M. Confined active species and effective charge separation in Bi₄O₅I₂ ultrathin hollow nanotube with increased photocatalytic activity. *Appl. Catal. B: Environ.* **2020**, *268*, 118403.

[14] Mao, D. J.; Yuan, J. L.; Qu, X. L.; Sun, C.; Yang, S. G.; He, H. Size tunable Bi₃O₄Br hierarchical hollow spheres assembled with {001}-facets exposed nanosheets for robust photocatalysis against phenolic pollutants. *J. Catal.* **2019**, *369*, 209–221.

[15] Xiong, J.; Song, P.; Di, J.; Li, H. M. Bismuth-rich bismuth oxyhalides: A new opportunity to trigger high-efficiency photocatalysis. *J. Mater. Chem. A* **2020**, *8*, 21434–21454.

[16] Jin, X. L.; Ye, L. Q.; Xie, H. Q.; Chen, G. Bismuth-rich bismuth oxyhalides for environmental and energy photocatalysis. *Coord. Chem. Rev.* **2017**, *349*, 84–101.

[17] Di, J.; Xia, J. X.; Ji, M. X.; Yin, S.; Li, H. P.; Xu, H.; Zhang, Q.; Li, H. M. Controllable synthesis of Bi₄O₅Br₂ ultrathin nanosheets for photocatalytic removal of ciprofloxacin and mechanism insight. *J. Mater. Chem. A* **2015**, *3*, 15108–15118.

[18] Dong, X. A.; Cui, Z. H.; Shi, X.; Yan, P.; Wang, Z. M.; Co, A. C.; Dong, F. Insights into dynamic surface bromide sites in Bi₄O₅Br₂ for sustainable N₂ photofixation. *Angew. Chem., Int. Ed.* **2022**, *61*, e202200937.

[19] Li, N.; Zhu, G. Q.; Hojamberdiev, M.; Zhu, R. L.; Chang, J.; Gao, J. Z.; Guo, Q. M.; Liu, P. Pd nanoparticle-decorated Bi₄O₅Br₂ nanosheets with enhanced visible-light photocatalytic activity for degradation of bisphenol A. *J. Photochem. Photobiol. A: Chem.* **2018**, *356*, 440–450.

[20] Wang, H. Y.; Zhou, Y.; Wang, J. N.; Li, A. M.; Corvini, P. F. X. BiOBr/Bi₄O₅Br₂/PDI constructed for visible-light degradation of endocrine disrupting chemicals: Synergistic effects of bi-heterojunction and oxygen evolution. *Chem. Eng. J.* **2022**, *433*, 133622.

[21] Zhu, G. Q.; Hojamberdiev, M.; Zhang, W. B.; Taj Ud Din, S.; Kim, Y. J.; Lee, J.; Yang, W. Enhanced photocatalytic activity of Fe-doped Bi₄O₅Br₂ nanosheets decorated with Au nanoparticles for pollutants removal. *Appl. Surf. Sci.* **2020**, *526*, 146760.

[22] Xiong, J.; Song, P.; Di, J.; Li, H. M.; Liu, Z. Freestanding ultrathin bismuth-based materials for diversified photocatalytic applications. *J. Mater. Chem. A* **2019**, *7*, 25203–25226.

[23] Bai, Y.; Yang, P.; Wang, L.; Yang, B.; Xie, H. Q.; Zhou, Y.; Ye, L. Q. Ultrathin Bi₄O₅Br₂ nanosheets for selective photocatalytic CO₂ conversion into CO. *Chem. Eng. J.* **2019**, *360*, 473–482.

[24] Xue, Y. H.; Zhang, Q.; Wang, W. J.; Cao, H.; Yang, Q. H.; Fu, L. Opening two-dimensional materials for energy conversion and storage: A concept. *Adv. Energy Mater.* **2017**, *7*, 1602684.

[25] Jin, X. L.; Lv, C. D.; Zhou, X.; Xie, H. Q.; Sun, S. F.; Liu, Y.; Meng, Q. Q.; Chen, G. A bismuth rich hollow Bi₄O₅Br₂ photocatalyst enables dramatic CO₂ reduction activity. *Nano Energy* **2019**, *64*, 103955.

[26] Mao, D. J.; Ding, S. S.; Meng, L. J.; Dai, Y. X.; Sun, C.; Yang, S. G.; He, H. One-pot microemulsion-mediated synthesis of Bi-rich Bi₄O₅Br₂ with controllable morphologies and excellent visible-light photocatalytic removal of pollutants. *Appl. Catal. B: Environ.* **2017**, *207*, 153–165.

[27] Zhao, W.; Yang, C. X.; Huang, J. D.; Jin, X. L.; Deng, Y.; Wang, L.; Su, F. Y.; Xie, H. Q.; Wong, P. K.; Ye, L. Q. Selective aerobic

oxidation of sulfides to sulfoxides in water under blue light irradiation over Bi₄O₅Br₂. *Green Chem.* **2020**, *22*, 4884–4889.

[28] Setvín, M.; Wagner, M.; Schmid, M.; Parkinson, G. S.; Diebold, U. Surface point defects on bulk oxides: Atomically-resolved scanning probe microscopy. *Chem. Soc. Rev.* **2017**, *46*, 1772–1784.

[29] Bai, X. J.; Wang, X. Y.; Jia, T. Q.; Guo, L. L.; Hao, D.; Zhang, Z. Y.; Wu, L. Y.; Zhang, X. R.; Yang, H.; Gong, Y. W. et al. Efficient degradation of PPCPs by Mo₁₋ₓS₂₋ᵧ with S vacancy at phase-junction: Promoted by innergenerate-H₂O₂. *Appl. Catal. B: Environ.* **2022**, *310*, 121302.

[30] Liu, Y. W.; Cheng, M.; He, Z. H.; Gu, B. C.; Xiao, C.; Zhou, T. F.; Guo, Z. P.; Liu, J. D.; He, H. Y.; Ye, B. J. et al. Pothole-rich ultrathin WO₃ nanosheets that trigger N≡N bond activation of nitrogen for direct nitrate photosynthesis. *Angew. Chem., Int. Ed.* **2019**, *58*, 731–735.

[31] Wu, Z. H.; Shen, J.; Ma, N.; Li, Z. F.; Wu, M.; Xu, D. F.; Zhang, S. Y.; Feng, W. H.; Zhu, Y. F. Bi₄O₅Br₂ nanosheets with vertical aligned facets for efficient visible-light-driven photodegradation of BPA. *Appl. Catal. B: Environ.* **2021**, *286*, 119937.

[32] Liu, G. P.; Wang, B.; Zhu, X. W.; Ding, P. H.; Zhao, J. Z.; Li, H. M.; Chen, Z. R.; Zhu, W. S.; Xia, J. X. Edge-site-rich ordered macroporous BiOCl triggers C=O activation for efficient CO₂ photoreduction. *Small* **2022**, *18*, 2105228.

[33] Wen, F. S.; Liu, W. L. Three-dimensional ordered macroporous materials for photocatalysis: Design and applications. *J. Mater. Chem. A* **2021**, *9*, 18129–18147.

[34] Cai, J. M.; Wu, M. Q.; Wang, Y. T.; Zhang, H.; Meng, M.; Tian, Y.; Li, X. G.; Zhang, J.; Zheng, L. R.; Gong, J. L. Synergetic enhancement of light harvesting and charge separation over surface-disorder-engineered TiO₂ photonic crystals. *Chem* **2017**, *2*, 877–892.

[35] Chen, X. Q.; Ye, J. H.; Ouyang, S. X.; Kako, T.; Li, Z. S.; Zou, Z. G. Enhanced incident photon-to-electron conversion efficiency of tungsten trioxide photoanodes based on 3D-photonic crystal design. *ACS Nano* **2011**, *5*, 4310–4318.

[36] Lin, B.; Yang, G. D.; Yang, B. L.; Zhao, Y. X. Construction of novel three dimensionally ordered macroporous carbon nitride for highly efficient photocatalytic activity. *Appl. Catal. B: Environ.* **2016**, *198*, 276–285.

[37] Chang, Y.; Yu, K.; Zhang, C. X.; Li, R.; Zhao, P. Y.; Lou, L. L.; Liu, S. X. Three-dimensionally ordered macroporous WO₃ supported Ag₃PO₄ with enhanced photocatalytic activity and durability. *Appl. Catal. B: Environ.* **2015**, *176–177*, 363–373.

[38] Wang, X. W.; Gan, L.; Lin, Q. Z.; Ye, S.; Zhang, R. B.; Liu, J. Micro-terminal regulation in nanoreactors for the construction of tantalum pentoxide single-crystal ordered networks with promoting enhanced hydrogen evolution performance. *Chem. Eng. J.* **2022**, *431*, 134139.

[39] Yu, K.; Zhang, C. X.; Chang, Y.; Feng, Y. J.; Yang, Z. Q.; Yang, T.; Lou, L. L.; Liu, S. X. Novel three-dimensionally ordered macroporous SrTiO₃ photocatalysts with remarkably enhanced hydrogen production performance. *Appl. Catal. B: Environ.* **2017**, *200*, 514–520.

[40] Wang, Z.; Hou, J. G.; Yang, C.; Jiao, S. Q.; Huang, K.; Zhu, H. M. Hierarchical metastable γ-TaON hollow structures for efficient visible-light water splitting. *Energy Environ. Sci.* **2013**, *6*, 2134–2144.

[41] Xie, S. H.; Liu, Y. X.; Deng, J. G.; Zhao, X. T.; Yang, J.; Zhang, K. F.; Han, Z.; Arandiyan, H.; Dai, H. X. Effect of transition metal doping on the catalytic performance of Au-Pd/3DOM Mn₂O₃ for the oxidation of methane and o-xylene. *Appl. Catal. B: Environ.* **2017**, *206*, 221–232.

[42] Pei, W. B.; Liu, Y. X.; Deng, J. G.; Zhang, K. F.; Hou, Z. Q.; Zhao, X. T.; Dai, H. X. Partially embedding Pt nanoparticles in the skeleton of 3DOM Mn₂O₃: An effective strategy for enhancing catalytic stability in toluene combustion. *Appl. Catal. B: Environ.* **2019**, *256*, 117814.

[43] Ran, L.; Qiu, S.; Zhai, P. L.; Li, Z. W.; Gao, J. F.; Zhang, X. M.; Zhang, B.; Wang, C.; Sun, L. C.; Hou, J. G. Conformal macroporous inverse opal oxynitride-based photoanode for robust photoelectrochemical water splitting. *J. Am. Chem. Soc.* **2021**, *143*, 7402–7413.

[44] Shu, C.; Han, C. Z.; Yang, X. Y.; Zhang, C.; Chen, Y.; Ren, S. J.; Wang, F.; Huang, F.; Jiang, J. X. Boosting the photocatalytic hydrogen evolution activity for D–π–A conjugated microporous polymers by statistical copolymerization. *Adv. Mater.* **2021**, *33*, 2008498.

[45] Wu, H.; Irani, R.; Zhang, K. F.; Jing, L.; Dai, H. X.; Chung, H. Y.; Abdi, F. F.; Ng, Y. H. Unveiling carrier dynamics in periodic porous BiVO₄ photocatalyst for enhanced solar water splitting. *ACS Energy Lett.* **2021**, *6*, 3400–3407.

[46] Wang, F. L.; Hou, T. T.; Zhao, X.; Yao, W.; Fang, R. Q.; Shen, K.; Li, Y. W. Ordered macroporous carbonous frameworks implanted with CdS quantum dots for efficient photocatalytic CO₂ reduction. *Adv. Mater.* **2021**, *33*, 2102690.

[47] Qiu, B. C.; Zhu, Q. H.; Du, M. M.; Fan, L. G.; Xing, M. Y.; Zhang, J. L. Efficient solar light harvesting CdS/Co₉S₈ hollow cubes for Z-scheme photocatalytic water splitting. *Angew. Chem., Int. Ed.* **2017**, *56*, 2684–2688.

[48] Hou, J. H.; Dai, D.; Wei, R.; Wu, X. G.; Wang, X. Z.; Tahir, M.; Zou, J. J. Narrowing the band gap of BiOCl for the hydroxyl radical generation of photocatalysis under visible light. *ACS Sustainable Chem. Eng.* **2019**, *7*, 16569–16576.

[49] Zhang, K. F.; Chen, H. X.; Liu, Y. X.; Deng, J. G.; Jing, L.; Rastegarpanah, A.; Pei, W. B.; Han, Z.; Dai, H. X. Two-dimensional Bi₂WₓMo₁₋ₓO₆ solution nanosheets for enhanced photocatalytic toluene oxidation to benzaldehyde. *Appl. Catal. B: Environ.* **2022**, *315*, 121545.

[50] Wang, J. L.; Yu, Y.; Zhang, L. Z. Highly efficient photocatalytic removal of sodium pentachlorophenate with Bi₃O₄Br under visible light. *Appl. Catal. B: Environ.* **2013**, *136–137*, 112–121.

[51] Di, J.; Xia, J. X.; Chisholm, M. F.; Zhong, J.; Chen, C.; Cao, X. Z.; Dong, F.; Chi, Z.; Chen, H. L.; Weng, Y. X. et al. Defect-tailoring mediated electron–hole separation in single-unit-cell Bi₃O₄Br nanosheets for boosting photocatalytic hydrogen evolution and nitrogen fixation. *Adv. Mater.* **2019**, *31*, 1807576.

[52] Wei, Z.; Wang, W. C.; Li, W. L.; Bai, X. Q.; Zhao, J. F.; Tse, E. C. M.; Phillips, D. L.; Zhu, Y. F. Steering electron–hole migration pathways using oxygen vacancies in tungsten oxides to enhance their photocatalytic oxygen evolution performance. *Angew. Chem., Int. Ed.* **2021**, *60*, 8236–8242.

[53] Tong, X. J.; Cao, X.; Han, T.; Cheong, W. C.; Lin, R.; Chen, Z.; Wang, D. S.; Chen, C.; Peng, Q.; Li, Y. D. Convenient fabrication of BiOBr ultrathin nanosheets with rich oxygen vacancies for photocatalytic selective oxidation of secondary amines. *Nano Res.* **2019**, *12*, 1625–1630.

[54] Han, T.; Cao, X.; Sun, K. A.; Peng, Q.; Ye, C. L.; Huang, A. J.; Cheong, W. C.; Chen, Z.; Lin, R.; Zhao, D. et al. Anion-exchange-mediated internal electric field for boosting photogenerated carrier separation and utilization. *Nat. Commun.* **2021**, *12*, 4952.

[55] Jing, J. F.; Yang, J.; Zhang, Z. J.; Zhu, Y. F. Supramolecular zinc porphyrin photocatalyst with strong reduction ability and robust built-in electric field for highly efficient hydrogen production. *Adv. Energy Mater.* **2021**, *11*, 2101392.

[56] Guo, Y.; Shi, W. X.; Zhu, Y. F. Internal electric field engineering for steering photogenerated charge separation and enhancing photoactivity. *EcoMat* **2019**, *1*, e12007.

[57] Liu, D.; Yao, W. Q.; Wang, J.; Liu, Y. F.; Zhang, M.; Zhu, Y. F. Enhanced visible light photocatalytic performance of a novel heterostructured Bi₄O₅Br₂/Bi₂₄O₃₁Br₁₀/Bi₂SiO₅ photocatalyst. *Appl. Catal. B: Environ.* **2015**, *172–173*, 100–107.

[58] Xiao, X.; Tu, S. H.; Lu, M. L.; Zhong, H.; Zheng, C. X.; Zuo, X. X.; Nan, J. M. Discussion on the reaction mechanism of the photocatalytic degradation of organic contaminants from a viewpoint of semiconductor photo-induced electrocatalysis. *Appl. Catal. B: Environ.* **2016**, *198*, 124–132.

[59] Zhang, L. L.; Wang, Z. Q.; Li, T.; Hu, C.; Yang, M. Ultrathin Bi₄O₅Br₂ nanosheets with surface oxygen vacancies and strong interaction with Bi₂O₂CO₃ for highly efficient removal of water contaminants. *Environ. Sci.: Nano* **2022**, *9*, 1341–1352.

[60] Ji, X. Y.; Wang, Y. Y.; Li, Y.; Sun, K.; Yu, M.; Tao, J. Enhancing photocatalytic hydrogen peroxide production of Ti-based metal–organic frameworks: The leading role of facet engineering. *Nano Res.* **2022**, *15*, 6045–6053.

[61] Zhang, K. F.; Liu, Y. X.; Deng, J. G.; Xie, S. H.; Zhao, X. T.; Yang, J.; Han, Z.; Dai, H. X. Co-Pd/BiVO$_4$: High-performance photocatalysts for the degradation of phenol under visible light irradiation. *Appl. Catal. B: Environ.* **2018**, *224*, 350–359.

[62] Mao, Y. S.; Wang, P. F.; Li, L. N.; Chen, Z. W.; Wang, H. T.; Li, Y.; Zhan, S. H. Unravelling the synergy between oxygen vacancies and oxygen substitution in BiO$_{2-x}$ for efficient molecular-oxygen activation. *Angew. Chem., Int. Ed.* **2020**, *59*, 3685–3690.

[63] Wang, T.; Tao, X. Q.; Xiao, Y.; Qiu, G. H.; Yang, Y.; Li, B. X. Charge separation and molecule activation promoted by Pd/MIL-125-NH$_2$ hybrid structures for selective oxidation reactions. *Catal. Sci.*

Technol. **2020**, *10*, 138–146.

[64] Zhou, Z. T.; Li, K. X.; Deng, W. Y.; Li, J.; Yan, Y. H.; Li, Y. W.; Quan, X. K.; Wang, T. Nitrogen vacancy mediated exciton dissociation in carbon nitride nanosheets: Enhanced hydroxyl radicals generation for efficient photocatalytic degradation of organic pollutants. *J. Hazard. Mater.* **2020**, *387*, 122023.

[65] Ji, J. H.; Yan, Q. Y.; Yin, P. C.; Mine, S.; Matsuoka, M.; Xing, M. Y. Defects on CoS$_{2-x}$: Tuning redox reactions for sustainable degradation of organic pollutants. *Angew. Chem., Int. Ed.* **2021**, *60*, 2903–2908.